SCIENCE CHINA Materials ARTICLES

mater.scichina.com link.springer.com

Published online 11 April 2019 | https://doi.org/10.1007/s40843-019-9416-7
Sci China Mater 2019, 62(8): 1139–1150

Stretchable SnO_2-CdS interlaced-nanowire film ultraviolet photodetectors

Ludong Li[1,2†], Zheng Lou[1†], Haoran Chen[1,2], Ruilong Shi[1,2] and Guozhen Shen[1,2*]

ABSTRACT **Stretchable ultraviolet photodetectors with fast response have wide applications in wearable electronics and implantable biomedical devices. However, most of the conventional binary oxide nanowires based photodetectors exhibit slow response due to the presence of a large number of surface defects related to trapping centers. Herein, with interlaced SnO_2-CdS nanowire films as the sensing materials, we fabricated stretchable ultraviolet photodetectors with significantly improved response speed *via* a multiple lithographic filtration method. Systematic investigations reveal that the interlaced-nanowire based photodetectors have lower dark current and much higher response speed (more than 100 times) compared with pure SnO_2 nanowire based photodetectors. The relevant carrier generation and transport mechanism were also discussed. In addition, due to the formation of waved wrinkles on the surface of the nanowires/PDMS layer during the prestretching cycles, the SnO_2-CdS interlaced nanowire photodetectors display excellent electrical stability and stretching cyclability within 50% strain, without obvious performance degradation even after 150 stretching cycles. As a simple and effective strategy to fabricate stretchable ultraviolet photodetectors with high response speed, the interlaced-nanowire structure can also be applied to other nanowire pairs, like ZnO-CdS interlaced-nanowires. Our method provides a versatile way to fabricate fast speed ultraviolet photodetectors by using interlaced metal oxide nanowires-CdS nanowires structures, which is potential in future stretchable and wearable optoelectronic devices.**

Keywords: stretchable electronics, interlaced-nanowire structure, nanowire photodetectors, SnO_2-CdS

INTRODUCTION

Stretchable electronics, as a kind of "soft" electronic devices which can be stretched, deformed and wrapped onto nonplanar curved surfaces, have attracted tremendous attraction due to their potential applications in wearable electronics, implantable biomedical devices, and artificial electronic skin [1–7]. So far, many types of stretchable electronic devices have been developed including stretchable transistors [8,9], light-emitting diodes (LEDs) [10,11], supercapacitors [12,13], photodetectors and sensors [14–17]. Ultraviolet (UV) photodetectors have wide applications in crime investigation, biological analysis, fire monitoring, and UV irradiation detection [18–21]. Stretchable UV photodetectors can be applied in much wider fields owing to their fascinating features of being stretchable, portable, implantable and wearable [4,14,15].

With wide bandgap, abundant reserves, large specific surface area, high aspect ratio and excellent stability, metal oxide nanowires (NWs) have been extensively studied as the active materials for high-performance UV photodetectors with much higher photoresponse compared with their bulk or thin-film counterparts [20–23]. Recently, researchers also tried to fabricate stretchable photodetectors with metal oxide NWs. For example, Wu *et al.* [24] synthesized buckled SnO_2 nanobelt webs and fabricated stretchable and transparent UV photodetectors. Ha *et al.* [25] fabricated stretchable UV sensor arrays with an average photosensitivity of ~10^5. Bhaskaran *et al.* [26] fabricated stretchable UV photodetectors with nanopatterned ZnO thin films as the sensing elements. Lee *et al.* [14] fabricated intrinsically stretchable ZnO NW photodetectors by embedding ZnO NWs in cured PDMS substrate. However, due to the presence of a large number of surface defects related to trapping centers, most of the reported UV photodetectors based on pure binary metal oxide NWs, stretchable or not, usually display a very low response speed, which greatly limits their practical applications [14,27–30].

[1] State Key Laboratory for Superlattices and Microstructures, Institute of Semiconductors, Chinese Academy of Sciences, Beijing 100083, China
[2] Center of Materials Science and Optoelectronics Engineering, University of Chinese Academy of Sciences, Beijing 100049, China
[†] These authors contributed equally to this paper.
[*] Corresponding author (email: gzshen@semi.ac.cn)

To improve the response speed of binary metal oxide based photodetectors, several attempts have been carried out [31–33]. For example, Morante *et al.* [31] reported that the decay time of the photodetectors based on monocrystalline ZnO NWs can be shortened by increasing either the probing current (self-heating by Joule dissipation) or the oxygen concentration in air (favouring the surface recombination mechanisms); Fan *et al.* [32] reported the photodetectors based on polycrystalline ZnO NWs with fast photoelectric response to low-intensity optical signal owing to barrier height modulation along the nanowire axial direction; Zhao *et al.* [33] fabricated the avalanche photodetectors based highly crystallized ZnO-Ga_2O_3 core-shell microwires, which displayed a very fast response speed duo to the avalanche gain mechanism. Considering the real-time response of photodetectors is very important for their applications in wearable electronics and implantable biomedical devices, it is highly desirable to find simple and effective ways to fabricate stretchable UV photodetectors with high response speed.

In this paper, we present an interesting SnO_2-CdS NW interlaced structure to fabricate stretchable UV photodetectors with fast response speed. Considering the high spectral responsivity of SnO_2 (direct E_g ~ 3.6 eV) NW photodetectors for UV light [27,34,35] and the fast response speed of CdS (direct E_g ~ 2.4 eV) NW photodetectors [36–39], the SnO_2 and CdS NWs were chosen to construct nanowires interlaced structure by a multiple lithographic filtration method to combine the merits of both materials. Systematic investigations on the photoresponse properties of the SnO_2-CdS interlaced NW photodetectors showed that they had lower dark current and much faster response speed compared with the SnO_2 NW photodetectors, and higher spectral responsivity compared with the CdS NW photodetectors in UV region. Waved wrinkles on the surface of the NWs/PDMS layer offered the device excellent electrical stability and stretching cyclability within 50% strain. This strategy can also be applied to other interlaced nanowire pairs like ZnO-CdS NWs. The above results indicate the nanowire interlaced structure may have broad applications in future stretchable and wearable optoelectronic devices.

EXPERIMENTAL SECTION

Synthesis of Ag NWs

The Ag NWs were synthesized by a solvothermal method, similar to the previous reports [40]. Briefly, 0.2 g polyvinylpyrrolidone (PVP) was dissolved in 20 mL ethylene glycol at 60°C to acquire homogeneous and transparent solution. 0.25 g $AgNO_3$ was then transferred to the above solution with magnetic stirring until it was completely dissolved. 3.5 g $FeCl_3$ solution (600×10^{-6} mol L^{-1} in ethylene glycol) was added into the above solution with magnetic stirring for 5 min. Finally, the mixed solution was poured into a Teflon-lined stainless steel autoclave (50 mL) followed by a solvothermal process under 130°C for 5 h. The obtained precipitates were collected and washed thrice with acetone and ethanol, respectively. The obtained Ag NWs were dispersed in ethanol with a concentration of 2.5 mg mL^{-1}.

Synthesis of CdS NWs

The CdS NWs were also grown *via* a solvothermal method. 0.62 g $Cd(NO_3)_2{\cdot}4H_2O$ was dissolved in 30 mL ethylenediamine ($C_2H_8N_2$) to form a homogeneous and transparent solution. 0.46 g thiourea ($SC(NH_2)_2$) was then added into the above solution with stirring. The mixed solution was transferred into a Teflon-lined stainless steel autoclave (50 mL) followed by a solvothermal process under 200°C for 16 h. The precipitates were collected and washed thrice with ethanol and deionized water, respectively. The obtained CdS NWs were dispersed in ethanol with a concentration of 2 mg mL^{-1}.

Synthesis of SnO_2 NWs

The SnO_2 NWs grew on Si substrate by a simple chemical vapor deposition method. In a typical process, 20 mg SnO powder was transferred to an alumina boat at the center of a tube furnace as the source. A Si(100) wafer coated with about 10 nm thick Au layer as the catalysts was then placed face-down above the source to ensure high vapor pressure and to collect the products. After the tube was purged with pure N_2 gas for 30 min, the tube furnace was heated to 920°C in 30 min and maintained at that temperature for 20 min. Upon elevating the furnace temperature, the N_2 gas with a flow rate of 300 sccm (standard cubic centimeters per minute) and the O_2 gas with a flow rate of 0.05 sccm were introduced into the tube furnace. After the reaction was completed, the tube furnace was cooled down to room temperature naturally. The obtained SnO_2 NWs on the Si substrate were put in ethanol and sonicated for 1 min to prepare the SnO_2 NWs solution (2 mg mL^{-1}).

Synthesis of ZnO NWs

The ZnO NWs were also synthesized on Si substrate *via* a chemical vapor deposition method. A mixture of 80 mg ZnO and 40 mg graphite powder was transferred to an alumina boat and placed at the center of a tube furnace.

The graphite powder was used for the carbothermal reduction of ZnO to generate Zn vapor. A Si (100) wafer coated with about 10 nm thick Au layer as the catalysts was then placed face-down to collect the growth products. After the tube was purged with pure N_2 gas for 30 min, the tube furnace was heated to 1,050°C in 35 min and maintained at that temperature for 2 h. N_2 gas with a flow rate of 100 sccm and the O_2 gas with a flow rate of 0.2 sccm were introduced into the tube furnace. The obtained ZnO NWs on the Si substrate were put in ethanol and sonicated for 1 min to prepare the ZnO NW solution (2 mg mL^{-1}).

Device fabrication

Two kinds of polydimethylsiloxane (PDMS) masks were first fabricated by the corresponding 3D printed molds which were printed out by a 3D printer. A moderate amount of PDMS liquid composed of a base and a curer (weight ratio 10:1) was injected into two 3D printed molds carefully *via* a pipette. After air bubbles disappeared, the PDMS liquid was thermally cured at 60°C for 4 h. Then, the two kinds of solid PDMS masks can be peeled off from the 3D printed molds. Mask I was prepared for Ag NW electrodes, and two masks II were prepared for SnO_2 and CdS NW channels, respectively. To fabricate the SnO_2-CdS interlaced NW photodetectors, the mask I was first placed on a polycarbonate (PC) filter membrane (Millipore GTTP, pore size 0.22 μm) to filter the Ag NW electrode pattern, and about 16 mL Ag NW ethanol solution was dripped into every vacancy in mask I. In a similar way, the SnO_2 and CdS NW channel patterns were filtered on the PC filter membrane in turn by the mask II, and about 10 mL corresponding NW ethanol solution was dripped into every vacancy in mask II. The PC filter membrane with Ag, SnO_2 and CdS NW patterns was then placed in a plastic culture dish (diameter ~5.5 mm). The PDMS liquid (about 1.3 mL) was injected on the top of the filter membrane. After liquid surface levelled and air bubbles disappeared, the PDMS liquid was thermally cured at 60°C for 4 h. Finally, the cured PDMS substrate was peeled off from the PC filter membrane with Ag, SnO_2 and CdS NW patterns transferred onto the PDMS matrix. The ZnO-CdS interlaced NW photodetectors were fabricated by a similar process, except that the SnO_2 NW ethanol solution was replaced by the ZnO NW ethanol solution. For the SnO_2, CdS and ZnO NW photodetectors, the NW patterns can be obtained by the first two-step filtration process, and every vacancy in mask II needed to occupy the whole electrode gap of Ag NW electrodes in the second filtration.

Material and device characterizations

The compositions and crystallinities of the as-synthesized NWs were analyzed *via* a powder X-ray diffractometer (Rigaku D/Max-2550, λ=1.5418 Å). The sizes and morphology of the NWs and devices were characterized by scanning electron microscopy (Zeiss Supra55 (VP)). The photoresponse of the devices were measured by the Keithley 4200-SCS semiconductor parameter analyzer linked to a probe station. A power-adjustable xenon lamp (CEL-HXUV300) was used as the illumination source for photoresponse measurements. The incident power of the light was measured by an Ophir NOVA power meter. The devices were fixed on a home-made stretching stage to apply strain. All the measurements were performed in air and at room temperature.

RESULTS AND DISCUSSION

The stretchable SnO_2-CdS interlaced NW photodetectors were fabricated by a multiple lithographic filtration method. Two pieces of PDMS masks with the thickness of ~1 mm were first made by a 3D printed mold which was printed out by a 3D printer, as shown in Fig. S1. Fig. S2a, b display the optical images of the as-fabricated mold I and mold II. To make it easier to peel off PDMS from the two molds, an Au layer with the thickness of 50 nm was deposited on their surfaces by thermal evaporation to reduce the surface roughness. The optical images of the corresponding PDMS mask I and PDMS mask II can be seen in Fig. S2c, d. Fig. 1a–e show the schematic illustration of the fabrication process of the stretchable SnO_2-CdS interlaced NW photodetectors array. First, the PDMS mask I for Ag NW electrodes was placed on the PC filter membrane (pore size 0.22 μm). Because of the vacuum suction force and sticky surface of PDMS, PDMS

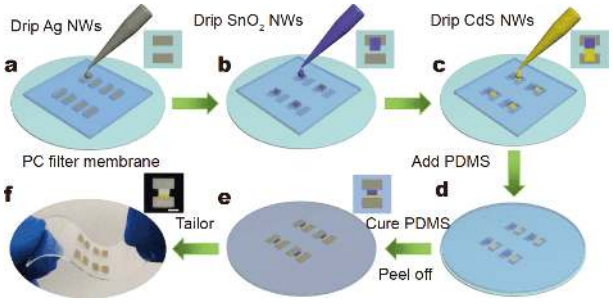

Figure 1 (a–e) Schematic illustration of the fabrication process of the stretchable SnO_2-CdS interlaced NW photodetectors array. (f) Optical image of the as-fabricated stretchable device arrays. The inset in (f) is an enlarged view of an individual device. The scale bar is 2 mm.

mask can closely contact with the filter membrane to prevent the diffusion of the NW solution and make well-defined patterns. Ethanol solution of Ag NWs was dripped into the electrode location and filtered to form a uniform NWs film (Fig. 1a). The size of the Ag NWs film is about 4 mm×2 mm, and the gap between the two Ag NW electrodes is about 1.5 mm. With a fixed NW concentration, the thickness of the NW film can be controlled by the volume of the NWs solution.

Then, the PDMS mask I was removed and the PDMS mask II for SnO_2 NWs was placed on the top of the patterned Ag NW electrodes. Every vacancy in PDMS mask II only occupied one Ag NW electrode and 2/3 of the electrode gap (Fig. 1b). The SnO_2 NW ethanol solution was dripped and filtered to form SnO_2 NWs pattern. The size of a SnO_2 NWs film is about 2 mm×2.5 mm. Following a similar process, the CdS NWs pattern was filtered on the top of Ag and SnO_2 NWs patterns. Every CdS NWs film occupied another Ag NW electrode and 2/3 of the electrode gap (Fig. 1c). After removing the PDMS mask II, the PC filter membrane with Ag, SnO_2 and CdS NWs patterns was placed in a plastic culture dish (diameter ~5.5 mm). Then, the PDMS liquid (about 1.3 mL) was injected on the top of the filter membrane (Fig. 1d), which can efficiently penetrate the porous NW films. After liquid surface levelled and air bubbles disappeared, the PDMS liquid was thermally cured at 60°C for 4 h. Finally, the cured PDMS substrate was peeled off from the PC filter membrane with Ag, SnO_2 and CdS NW patterns transferred onto the PDMS matrix (Fig. 1e).

Fig. 1f shows the optical image of the as-fabricated stretchable SnO_2-CdS interlaced NW photodetectors array. The inset of Fig. 1f is an enlarged view of an individual device, which consists of two symmetric Ag NW electrodes and one SnO_2-CdS interlaced NW detection channel. Fig. S3 displays the scanning electron microscopy (SEM) images of the Ag, SnO_2 and CdS NWs for the fabrication of the stretchable SnO_2-CdS interlaced NW photodetectors, respectively. The diameters of the as-synthesized Ag, SnO_2 and CdS NWs are 50–100, 100–200, and 40–50 nm, respectively. Induced by the tendency to lower the surface free energy, the CdS NWs aggregated into NW bundles to reduce the exposed areas during the growth [41,42]. Fig. S4 displays the XRD patterns of the as-synthesized Ag, SnO_2 and CdS NWs, revealing they are face-centered cubic Ag (JCPDS Card No. 04-0783), tetragonal rutile SnO_2 (JCPDS Card No. 41-1445), and hexagonal wurtzite CdS (JCPDS Card No. 65-3414), respectively.

Fig. 2a shows the schematic cross-sectional view of the SnO_2-CdS interlaced NW photodetector, where two Ag NW electrodes are on the top of SnO_2 and CdS NW layers, respectively. Between the two Ag NW electrodes, the detection channel is composed of SnO_2 area, SnO_2/CdS overlapping area, and CdS area. SEM image of the as-fabricated device was displayed in Fig. 2b, consistent with the device schematic diagram in Fig. 2a. Fig. 2b also shows that there are some wrinkles in the NW layer,

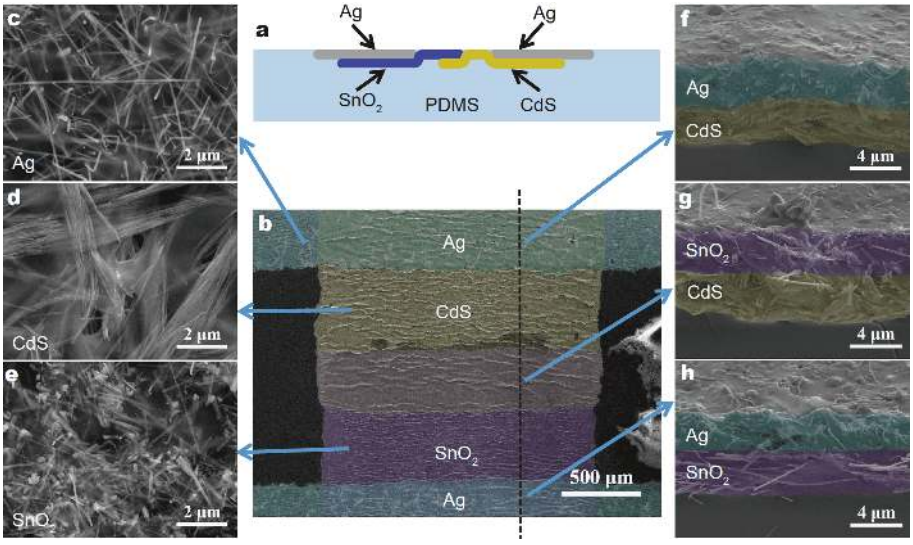

Figure 2 (a) Schematic cross-sectional view of the stretchable SnO_2-CdS interlaced NWs photodetector. (b) Top-view SEM image of the stretchable SnO_2-CdS interlaced NWs photodetector. (c–e) SEM views of the Ag, CdS and SnO_2 NWs embedded in PDMS substrate. (f–h) Cross-sectional SEM images of the Ag/CdS, SnO_2/CdS, and Ag/SnO_2 NWs overlapping areas, respectively.

which can be ascribed to the residual strain causing by the irreversible sliding of NWs in the PDMS substrate during the device peeling process [14,43]. Due to the difference in NWs film thickness, the Young's modulus, the Poisson's ratio, and the applied strain, the amplitude and wavelength of the wrinkles are different [12], which makes it easier to recognize the three areas of the detection channel. Fig. 2c–e display the enlarged SEM images of the Ag, CdS and SnO_2 NW areas of the photodetector, respectively, where the Ag, CdS and SnO_2 NWs are embedded in the PDMS substrate. Fig. 2f–h show the cross-sectional SEM images of the Ag/CdS, SnO_2/CdS, and Ag/SnO_2 NWs overlapping areas, respectively. A clear bilayer structure can be found in the NWs overlapping areas. The relative positions of the Ag, CdS and SnO_2 NWs layers are corresponding to the device schematic diagram in Fig. 2a. The thickness ranges of the Ag, CdS and SnO_2 NW layers are all about 2.8–3.6 μm. For the Ag, CdS and SnO_2 NWs layers are fully embedded in the PDMS substrate, all the components of the photodetector can be stretched.

The photoresponse characteristics of the as-fabricated SnO_2-CdS interlaced NWs photodetectors were investigated systematically. For comparison, photodetectors with pure SnO_2 NWs and pure CdS NWs were also fabricated. Fig. 3a shows the spectral responsivity of the SnO_2-CdS interlaced NWs device, the SnO_2 NWs device, and the CdS NWs device at different wavelengths ranging from 250 to 650 nm at a bias voltage of 5 V, respectively. The spectral responsivity is a key figure-of-merit of photodetectors, which can be defined as:

$$R_\lambda = \Delta I / PS = \left(I_{\text{light}} - I_{\text{dark}}\right) / PS, \quad (1)$$

where I_{light} is the light current, I_{dark} is the dark current, P is the incident light intensity, and S is the effective irradiated area [21]. The spectral responsivity of the SnO_2 NWs photodetector mainly focuses on the ultraviolet (UV) region (<390 nm) and the peak is at 310 nm, due to the wide bandgap of SnO_2 (direct E_g ~ 3.6 eV) [8,34,35]. Owing to the relatively narrow bandgap (direct E_g ~ 2.4 eV), the spectral responsivity of the CdS NW photodetector focuses on both UV and visible regions (<550 nm) and the peak is at 510 nm [36–39]. As for the spectral responsivity of the SnO_2-CdS interlaced NWs photodetector, the spectral responsivity mainly locates in both the UV and the visible regions (<550 nm) with a peak at 370 nm. As the detection channel of the interlaced NWs device is composed of both SnO_2 and CdS NWs with an interlaced structure, its spectral responsivity is mainly decided by the combined effect of both SnO_2 and CdS NWs. It is well known that, in the combined effect,

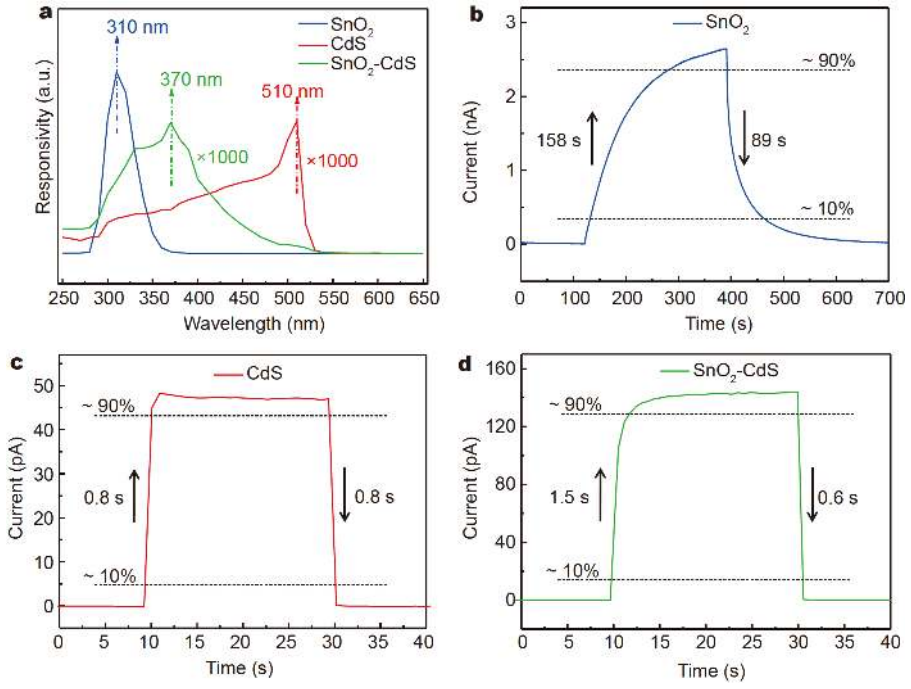

Figure 3 (a) Spectral responsivity of three kinds of photodetectors at different wavelengths ranging from 250 to 650 nm at a bias voltage of 5 V. (b–d) *I-t* curves of the three kinds of devices during on-off switching under 370 nm UV illumination with a light intensity of 11.64 mW cm^{-2}, the bias voltage is 5 V.

the one with smaller value usually is the dominating factor. From the above results, the spectral responsivity of SnO_2 NWs device increases from 510 to 310 nm, while it decreases for CdS NWs device. As a result, from 510 to 310 nm, for the SnO_2-CdS interlaced NW device, its spectral responsivity first increases, reaches the peak at 370 nm, and then decreases. Fig. S5 shows the *I-V* curves of the SnO_2-CdS interlaced NWs device, the SnO_2 NWs device, and the CdS NWs device in dark and under 370 nm UV illumination with a light intensity of 11.64 mW cm^{-2}, respectively. The linear and symmetric light current curves of all the three devices indicate good Ohmic contact, which is caused by the fact that the work function of Ag (Φ_{Ag} = 4.26 eV) is close to the electron affinities of both SnO_2 (χ_{SnO_2} = 4.5 eV) and CdS (χ_{CdS} = 3.98 eV) [44,45]. At a bias voltage of 5 V, the light currents of the SnO_2 device, the CdS device and the SnO_2-CdS device are 2.7 nA, 47.7 pA and 142.4 pA, and the dark currents are 3.0 pA, 18.5 fA and 19.2 fA, respectively. Thus, the light-to-dark current ratios (I_{light}/I_{dark}) of the corresponding three devices are 900, 2,578 and 7,417, respectively.

Response speed is one of the key parameters of photodetectors. We also studied the response speed of the above fabricated three kinds of photodetectors. Fig. 3b–d displayed the corresponding *I-t* curves during on-off switching under 370 nm UV illumination with a light intensity of 11.64 μW cm^{-2} at a bias voltage of 5 V, respectively. For the SnO_2 NWs photodetector, the rise time and decay time are about 158 and 89 s, respectively. Here, the rise time and decay time are defined as the time needed for current transition from 10% to 90% (or 90% to 10%) of the steady-state photocurrent. The extremely slow response of the SnO_2 device made it unsuitable for practical application. For the CdS NWs photodetector, both the rise time and the decay time are about 0.8 s, much faster than those of the SnO_2 device. Caused by the combined effect of both SnO_2 NWs and CdS NWs, the SnO_2-CdS NWs device shows fast rise and decay time of 1.5 and 0.6 s, respectively.

The above results reveal that the SnO_2-CdS interlaced NWs photodetectors have lower dark current and much faster response speed compared with pure SnO_2 device, and higher spectral responsivity compared with pure CdS device in UV region. The corresponding mechanisms can be explained as follows. Due to the large specific surface area of NWs, the photoresponse behaviors of NW photodetectors are mainly based on the photoexcitation processes associated with the adsorption and desorption of oxygen [14,22–32]. Because PDMS is a gas-permeable elastomer with an air solubility of about 15.4 vol% (25°C, 1 atm) [14,46], the photoresponse behaviors of the NWs photodetectors embedded in PDMS substrate are also influenced by the oxygen adsorption and desorption on the surface of NWs. In dark condition, oxygen adsorbed on the surface of SnO_2 and CdS NWs can capture free electrons *via*:

$$O_2(g) + e^- \rightarrow O_2^-(ad). \quad (2)$$

A depletion layer forms at the surface of the NWs, which builds an internal electric field in radial direction, and thus induces surface band bending upwards [31,32]. Correspondingly, a back-to-back barrier forms at the interface of the two NWs [47], as shown in Fig. 4a. Due to the difference between the electron affinities of SnO_2 and CdS (about 0.52 eV), the back-to-back heterojunction barriers between SnO_2 NWs and CdS NWs are higher than their back-to-back homojunction barriers [44]. At the same bias voltage of 5 V, obvious difference of dark currents of the SnO_2 NWs photodetector (3.0 pA) and the CdS NWs photodetector (18.5 fA) reveals that CdS NWs have a higher resistance compared with SnO_2 NWs. Because of the high resistance of CdS and the back-to-back heterojunction barriers between SnO_2 and CdS NWs, the SnO_2-CdS interlaced NWs photodetector displays a very low dark current of 19.2 fA, which is similar with the dark current of the CdS NWs photodetector. Under UV illumination, a large amount of electron-hole pairs are generated in both SnO_2 and CdS NWs through (Fig. 4b):

$$h\nu \rightarrow e^- + h^+. \quad (3)$$

The negative oxygen ions adsorbed on the surface of NWs trap the photo-generated holes *via* the following equation and desorb from the surface of the NWs, which reduces the surface band bending of NWs, resulting in the lowered barrier height (Fig. 4c):

$$O_2^-(ad) + h^+ \rightarrow O_2(g). \quad (4)$$

Thus, the electrons can easily transport across these barriers by tunneling and thermionic emission at a bias voltage, leading to a significantly increased light current. Due to the high spectral responsivity of SnO_2 NWs under UV illumination (Fig. 3a), much more photo-generated electrons are generated in SnO_2 NWs layer and transported into the CdS NWs layer (Fig. 4c). The increased electron concentration in the SnO_2-CdS interlaced NWs photodetector makes it display a higher light current and spectral responsivity compared with the CdS NWs photodetector in UV region. And for the CdS NWs layer, the rise speed is fast, as confirmed in Fig. 3c. Because of the high resistance of CdS NWs layer, the steady-state light

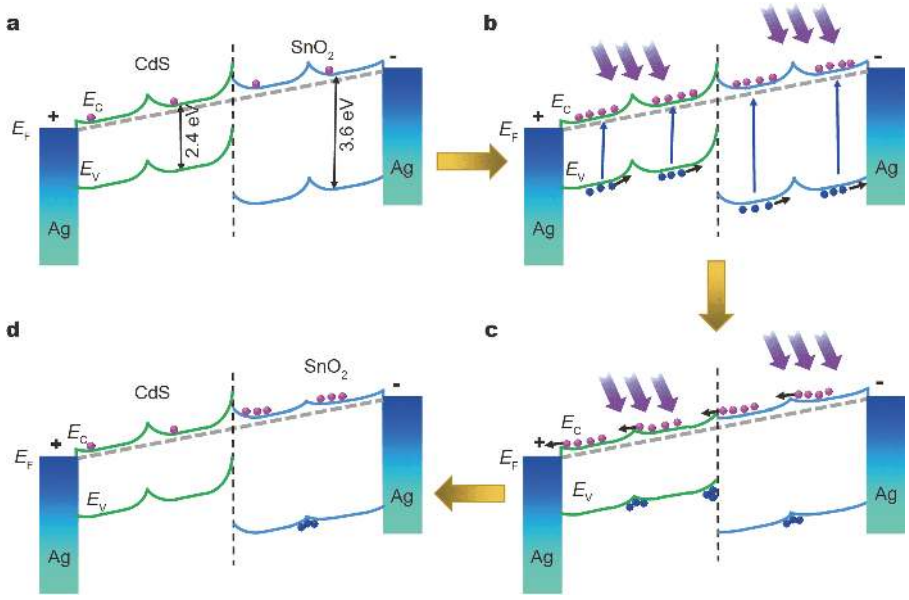

Figure 4 Energy band diagrams of carriers generation and transport mechanisms in the SnO_2-CdS interlaced NWs photodetector in the dark (a, d) and under UV illumination (b, c). The Ag NWs electrode near the CdS NWs is at a positive bias voltage.

current of the SnO_2-CdS interlaced NWs photodetector is still much lower than that of the SnO_2 NWs photodetector (Fig. 3d). Although the SnO_2 NWs layer has a slow rise speed, the rise time required from the dark current to the current value of the steady-state light current of the SnO_2-CdS interlaced NWs photodetector is still very short due to the high spectral responsivity of SnO_2 NWs under UV illumination. As a result, the rise speed of the SnO_2-CdS interlaced NWs photodetector is a little slower than that of CdS NWs photodetector, but much faster (about 100 times) than that of SnO_2 NWs photodetector. When the UV illumination is turned off, the CdS NWs layer recovers to the initial state quickly, as confirmed in Fig. 3c. The residual electrons in the SnO_2 NWs layer cannot transport into the CdS NWs layer because of the barrier height of the back-to-back heterojunction barriers between SnO_2 and CdS NWs (Fig. 4d). The high resistance of CdS NWs and the back-to-back heterojunction barriers make the SnO_2-CdS interlaced NWs photodetector recover to the initial dark current rapidly with a decay speed similar with that of CdS NWs photodetector. In the case of Fig. 4, the Ag NWs electrode near the CdS NWs is at a positive bias voltage. The energy band diagrams with a reverse bias voltage are shown in Fig. S6. The carrier generation and transport mechanisms are similar except that the electrons transport from the CdS NWs layer to the SnO_2 NWs layer.

For a stretchable device, the electrical stability under stretching condition is a very important parameter to evaluate its potential for practical applications. We also measured the corresponding performance of the stretchable SnO_2-CdS interlaced NWs photodetectors. To measure the stretching performance, the device was fixed on a home-built stretching stage. The required strain can be applied by adjusting the distance between two ends of the stretching stage. Here the strain is defined as:

$$\text{Strain} = (L - L_0)/L_0, \quad (5)$$

where L_0 and L are the lengths of the stretchable device before and after stretching, respectively. Fig. 5a displays the optical images of the as-fabricated stretchable device at 0% and 50% strain, respectively, indicating a good stretchability of the device. It should be noticed that, in this work, we found that a prestretching process is very important for the electrical stability of the as-fabricated stretchable NWs photodetectors under stretching condition.

Fig. S7 shows the light current variation of the stretchable device at 0% and 50% strain during the first 5 prestretching cycles. The whole process that the device is stretched from 0% to 50% and then released to 0% is defined as one stretching cycle. It can be seen that the light current at 0% and 50% strain decreases during the first two prestretching cycles, and then reaches to the same value and keeps almost unchanged during the fol-

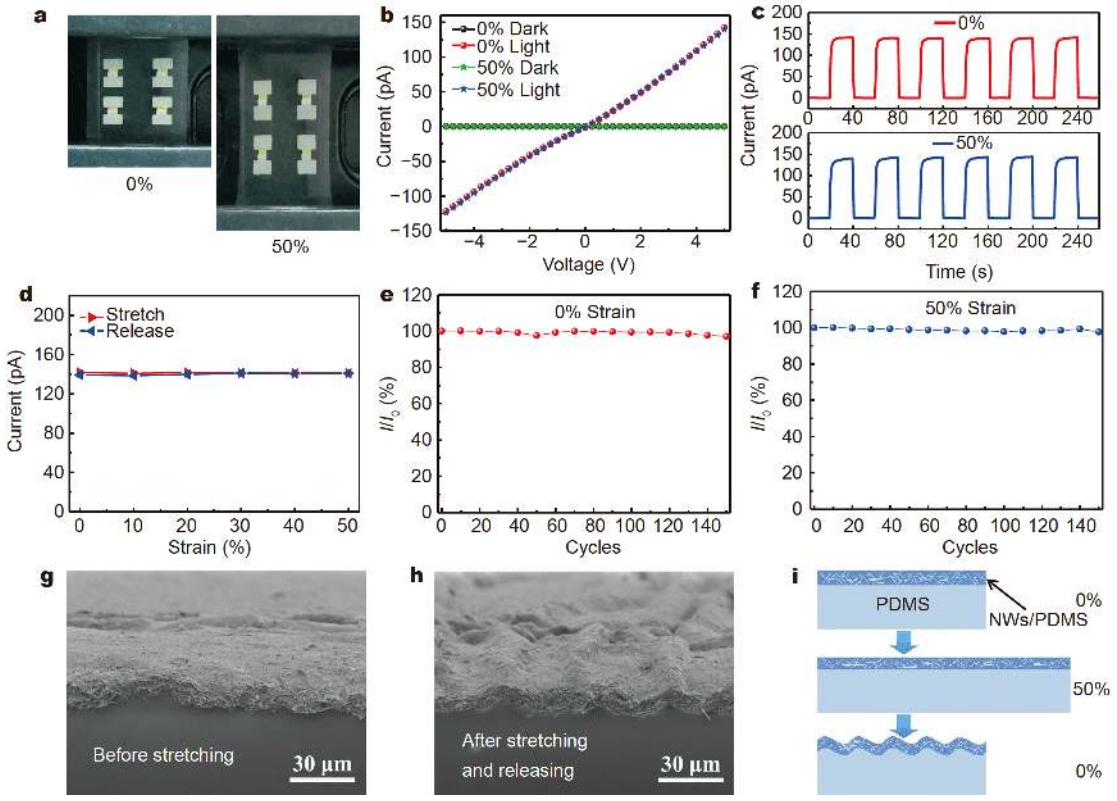

Figure 5 (a) Optical images, (b) *I-V* curves, (c) dynamic *I-t* curves, and (d) light current variation of the as-fabricated stretchable devices at 0% and 50% strain, respectively. (e, f) Light current retentions of the stretchable photodetector at 0% and 50% strain after different cycles of stretching, respectively. (g, h) Cross-sectional SEM images of the NWs/PDMS layer before stretching and after prestretching cycles. (i) Schematic illustration of the deformation of the NWs/PDMS layer during the stretching and releasing process.

lowing three prestretching cycles. To verify the effect of prestretching process, the electrical stability of the stretchable device was then further measured after 5 prestretching cycles. Fig. 5b shows the *I-V* curves of the stretchable device at 0% and 50% strain in the dark and under UV light (370 nm, 11.64 μW cm^{-2}). With a 50% strain, both the *I-V* curves of the stretchable device in dark and under UV light are almost identical to the *I-V* curves without stretching.

The dynamic *I-t* curves of the stretchable device at 0% and 50% strain after prestretching cycles are displayed in Fig. 5c. For the dynamic *I-t* curve at 50% strain, there is no obvious change of the light currents for the given six cycles, as well as the dynamic *I-t* curve at 0% strain, revealing the superior reproducibility and stability of the stretchable device. The rise time and decay time of the stretchable device at 0% and 50% strain are similar. Fig. 5d shows the light current variation of the stretchable photodetector at different strains from 0% to 50%. During the whole process, the light currents of the device remain nearly constant, further indicating the outstanding electrical stability of the as-fabricated stretchable NWs photodetectors. Fig. 5e, f display the light current retentions of the stretchable photodetector at 0% and 50% strain after different cycles of stretching. After 5 prestretching cycles, the light currents of the stretchable photodetector at 0% and 50% strain show a good stability during the following stretching cycle measurement. Even after 150 stretching cycles, both the light currents of the stretchable photodetector at 0% and 50% strain still retain 97% of the initial value, revealing the excellent stretching cyclability of the as-fabricated stretchable NWs photodetectors.

The above results further confirm that the stretchable NWs photodetectors can obtain superior electrical stability and stretching cyclability after a prestretching process. To investigate the mechanism of the effect of prestretching process, the surface morphology of the NWs/PDMS layer was characterized using SEM. Fig. 5g shows the cross-sectional SEM image of the NWs/PDMS layer before stretching. The surface of the NWs/PDMS layer is nearly flat, and the slight fluctuations are mainly caused by the device peeling process. Fig. 5h displays the

cross-sectional SEM image of the NWs/PDMS layer after 5 prestretching cycles. A top view of the NWs/PDMS surface after 5 prestretching cycles can be seen in Fig. S8. Many waved wrinkles are on the surface of the NWs/PDMS layer along the stretching direction, in contrast to the nearly flat surface before stretching.

Fig. 5i shows the schematic illustration of the deformation of the NWs/PDMS layer during the stretching and releasing process. When the NWs/PDMS layer was first stretched, NWs embedded in the PDMS substrate might slide between each other due to the strain [14,43]. Because the conductivity of the NWs network is dramatically influenced by the contacts between NWs [43,48], the conductivity of the NWs/PDMS layer decreases obviously during the first stretching process due to the weakening and detachment of the NWs contacts, as confirmed in Fig. S7. However, when the NWs/PDMS layer is released, the NWs cannot slide back to the initial state because of the friction force between the NWs and the PDMS substrate [43]. As a result, many waved wrinkles appear on the surface of the NWs/PDMS layer due to the residual strain caused by the irreversible sliding of NWs in the PDMS substrate [14,42]. The phenomena of irreversible fiber arrangement and residual strain also was found in many other fiber networks [49,50]. For the second stretching cycle, the flattening of the waved wrinkles can release most of the strain and reduce the sliding of NWs between each other, so the conductivity of the NWs/PDMS layer only slightly decreases, as shown in Fig. S7. After several prestretching cycles, the sliding of NWs in the PDMS substrate can gradually reach saturation for the 50% strain. Consequently, for the following stretching cycles within 50% strain, the stretching process is just the flattening of the waved wrinkles in the NWs/PDMS layer, leading to the stable conductivity of the NWs/PDMS layer during the stretching process. Thus, the stretchable NWs photodetectors can obtain excellent electrical stability and stretching cyclability after a prestretching process.

By design of the NWs interlaced structure, the performance of the stretchable SnO_2-CdS NWs photodetectors can be easily tuned. For example, our above results demonstrate that the interlaced devices display lower dark current and much faster response speed compared with the SnO_2 device, and higher spectral responsivity compared with the CdS device. In fact, the NWs interlaced structure can be easily expanded to many other oxide NWs photodetectors to achieve similar effect. Due to the different bandgaps of different oxide NWs, the peak response wavelength of the interlaced NWs photodetectors can be adjusted easily by changing oxide NWs. Herein, to demonstrate the NWs interlaced structure for other oxide NW photodetectors, stretchable ZnO-CdS interlaced NWs photodetectors were fabricated *via* a similar fabrication process in Fig. 1a–e, except that the SnO_2 NWs ethanol solution was replaced by the ZnO NWs ethanol solution in the step of Fig. 1b.

Fig. 6a shows the optical image of the as-fabricated stretchable ZnO-CdS interlaced NWs photodetectors array. The inset in Fig. 6a is an enlarged view of an individual device, which also consists of two symmetric Ag NWs electrodes and one ZnO-CdS interlaced NWs detection channel. The ZnO NWs used for the ZnO-CdS interlaced NWs photodetectors were synthesized by a simple chemical vapor deposition method, and the detail of synthesis process can be found in the Supplementary information. Fig. S9 shows the different magnification SEM images of the as-synthesized ZnO NWs. Many freestanding NWs were synthesized on the substrate, with a length of dozens of micrometers and a diameter of 100–200 nm. Fig. S10 displays the XRD pattern of the as-synthesized ZnO NWs, indicating the NWs are pure hexagonal wurtzite ZnO phase (JCPDS Card No. 36-1451). The photoresponse characteristics of the ZnO-CdS interlaced NWs photodetector were then investigated and the pure ZnO NWs based device was also fabricated for comparison. Fig. 6b shows the spectral responsivity of the ZnO-CdS interlaticed NWs device, the ZnO NWs device, and the CdS NWs device at different wavelengths ranging from 250 to 650 nm at a bias voltage of 5 V. The spectral responsivity of the ZnO NWs device mainly lies in the UV region (<430 nm) due to the wide bandgap of ZnO (direct E_g ~ 3.2 eV) [28,32]. The peak is at 380 nm, which can be attributed to the fact that the bandgap of ZnO is smaller than that of SnO_2 (direct E_g ~ 3.6 eV). Because of the narrower bandgap of CdS NWs, the spectral responsivity of the ZnO-CdS interlaced NWs device lies in both the UV and visible regions (<550 nm). The peak of the ZnO-CdS interlaced NWs device is at 380 nm, same with the peak wavelength of the ZnO NWs photodetector. This interesting phenomenon can be attributed to the very high spectral responsivity of ZnO NWs at 380 nm and the spectral responsivity of CdS NWs is not low enough at 380 nm. As a result, the combined effect of the spectral responsivity of ZnO NWs and CdS NWs can still reach the maximum value at 380 nm, similar to the above discussed SnO_2 and CdS NWs. Besides, the ZnO-CdS interlaced NWs device shows a much higher responsivity (about 9 times) than that of the pure CdS NWs device, as shown in Fig. 6b.

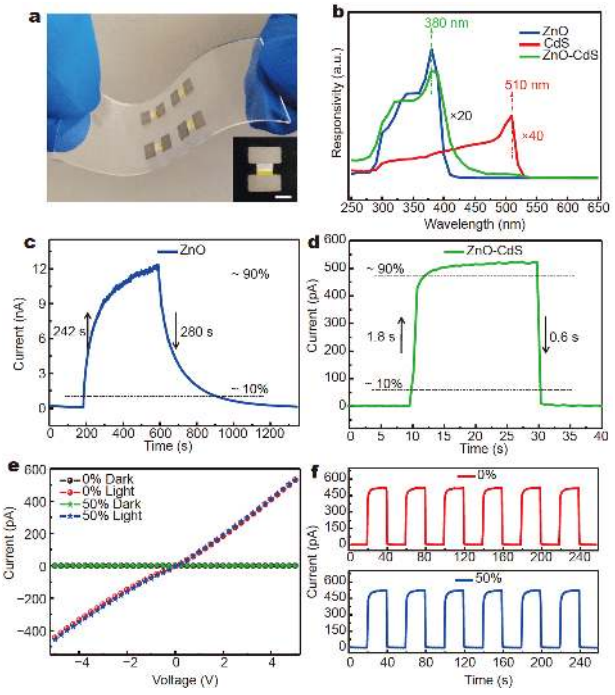

Figure 6 (a) Optical image of the as-fabricated stretchable ZnO-CdS interlaced NWs photodetectors array. The inset in (a) is an enlarged view of an individual device. The scale bar is 2 mm. (b) Spectral responsivity of the ZnO-CdS interlaticed NWs device, the ZnO NWs device, and the CdS NWs device at different wavelengths ranging from 250 to 650 nm at a bias voltage of 5 V, respectively. (c, d) *I-t* curves of the ZnO-CdS interlaticed NWs device, and the ZnO NWs device during on-off switching under 380 nm UV illumination with a light intensity of 12.22 μW cm^{-2}. (e) *I-V* curves of the stretchable ZnO-CdS interlaced NWs photodetectors at 0% and 50% strain. (f) Dynamic *I-t* curves of the stretchable ZnO-CdS interlaced NWs devices at 0% and 50% strain with periodic UV illumination.

Fig. 6c depicts the *I-t* curve of the pure ZnO NWs device during on-off switching under 380 nm UV illumination with a light intensity of 12.22 μW cm^{-2} at a bias voltage of 5 V. The response speed of the ZnO NWs photodetector is very slow, similar to the pure SnO_2 NWs device in Fig. 3b. The rise time and decay time of the ZnO NWs photodetector are about 242 and 280 s, respectively. By design of the ZnO-CdS interlaced NWs device, as shown in Fig. 6d, the rise time and decay time can be drastically decreased to about 1.8 and 0.6 s, respectively. The rise speed is also a little slower than that of CdS NWs device (Fig. 3c), but much faster (about 130 times) than that of ZnO NWs device. Similarly, the decay speed is similar with that of the CdS NWs device, but much faster (about 460 times) than that of ZnO NWs device. The relevant carrier generation and transport mechanism of the ZnO-CdS interlaced NWs photodetectors are similar with the SnO_2-CdS interlaced NWs photodetectors discussed in Fig. 4. Due to the high resistance of CdS NWs and the back-to-back heterojunction barriers between ZnO and CdS NWs, the ZnO-CdS interlaced NWs photodetectors also display a very low dark current of 18.0 fA at a bias voltage of 5 V, which is much smaller than the dark current of the ZnO NWs device (3.1 pA). Under a 380 nm UV light illumination, the light currents of the ZnO-CdS and ZnO NWs photodetectors are 531.1 pA and 12.2 nA, respectively. The light-to-dark current ratio of the ZnO-CdS interlaced NWs device (29,505) is much higher (about 7 times) than that of the ZnO NWs device (3,935).

The electrical stability of the ZnO-CdS interlaced NWs device under stretching condition was also measured after 5 prestretching cycles. *I-V* curves of the stretchable device at 0% and 50% strain in dark and under UV light (380 nm, 12.22 μW cm^{-2}) after prestretching cycles are shown in Fig. 6e. At a 50% strain, the *I-V* curves of the stretchable device in dark and under UV light illumination are almost the same with the *I-V* curves at a 0% strain. Fig. 6f shows the dynamic *I-t* curves of the stretchable ZnO-CdS interlaced NWs device at 0% and 50% strain with periodic UV illumination. At a bias voltage of 5 V, the *I-t* curves of the stretchable device at 0% and 50% strain show nearly identical light and dark currents and rise and decay times for the given six cycles, revealing the outstanding electrical stability of the as-fabricated stretchable ZnO-CdS interlaced NWs photodetectors.

CONCLUSIONS

In conclusion, we presented a SnO_2-CdS NWs interlaced structure to fabricate stretchable UV photodetectors with fast response speed by a multiple lithographic filtration method. Systematic investigations were carried out to study the photoresponse characteristics of the as-fabricated stretchable devices. The results reveal that the SnO_2-CdS interlaced NWs device has lower dark current (as low as 19.2 fA) and much faster response speed (more than 100 times) compared with the pure SnO_2 NWs device, and higher spectral responsivity compared with the pure CdS NWs device. In addition, the SnO_2-CdS interlaced NWs photodetectors exhibit excellent electrical stability and stretching cyclability within 50% strain after 5 prestretching cycles, which can be attributed to the formation of waved wrinkles on the surface of the NWs/PDMS layer during the prestretching cycles. As a simple and effective strategy to fabricate stretchable UV photodetectors with fast response speed, the NWs interlaced

structure can also be applied to other NWs pairs like ZnO-CdS NWs. We believe that this strategy may further promote the development of future stretchable and wearable optoelectronic devices.

Received 18 February 2019; accepted 14 March 2019; published online 11 April 2019

1 Sekitani T, Someya T. Stretchable, large-area organic electronics. Adv Mater, 2010, 22: 2228–2246
2 Rogers JA, Someya T, Huang Y. Materials and mechanics for stretchable electronics. Science, 2010, 327: 1603–1607
3 Hammock ML, Chortos A, Tee BCK, *et al.* 25th Anniversary article: The evolution of electronic skin (e-skin): a brief history, design considerations, and recent progress. Adv Mater, 2013, 25: 5997–6038
4 Lou Z, Shen G. Flexible photodetectors based on 1D inorganic nanostructures. Adv Sci, 2016, 3: 1500287
5 Trung TQ, Lee NE. Recent progress on stretchable electronic devices with intrinsically stretchable components. Adv Mater, 2017, 29: 1603167
6 Le VQ, Do TH, Retamal JRD, *et al.* van der Waals heteroepitaxial AZO/NiO/AZO/muscovite (ANA/muscovite) transparent flexible memristor. Nano Energy, 2019, 56: 322–329
7 Ai Y, Hsu TH, Wu DC, *et al.* An ultrasensitive flexible pressure sensor for multimodal wearable electronic skins based on large-scale polystyrene ball@reduced graphene-oxide core–shell nanoparticles. J Mater Chem C, 2018, 6: 5514–5520
8 Cai L, Zhang S, Miao J, *et al.* Fully printed stretchable thin-film transistors and integrated logic circuits. ACS Nano, 2016, 10: 11459–11468
9 Oh JY, Rondeau-Gagné S, Chiu YC, *et al.* Intrinsically stretchable and healable semiconducting polymer for organic transistors. Nature, 2016, 539: 411–415
10 Kim RH, Kim DH, Xiao J, *et al.* Waterproof AlInGaP optoelectronics on stretchable substrates with applications in biomedicine and robotics. Nat Mater, 2010, 9: 929–937
11 Yu Z, Niu X, Liu Z, *et al.* Intrinsically stretchable polymer light-emitting devices using carbon nanotube-polymer composite electrodes. Adv Mater, 2011, 23: 3989–3994
12 Yu C, Masarapu C, Rong J, *et al.* Stretchable supercapacitors based on buckled single-walled carbon-nanotube macrofilms. Adv Mater, 2009, 21: 4793–4797
13 Li L, Lou Z, Han W, *et al.* Highly stretchable micro-supercapacitor arrays with hybrid MWCNT/PANI electrodes. Adv Mater Technol, 2017, 2: 1600282
14 Yan C, Wang J, Wang X, *et al.* An intrinsically stretchable nanowire photodetector with a fully embedded structure. Adv Mater, 2014, 26: 943–950
15 Wang J, Yan C, Kang W, *et al.* High-efficiency transfer of percolating nanowire films for stretchable and transparent photodetectors. Nanoscale, 2014, 6: 10734–10739
16 Yoo J, Jeong S, Kim S, *et al.* A stretchable nanowire UV-vis-NIR photodetector with high performance. Adv Mater, 2015, 27: 1712–1717
17 Chiang CW, Haider G, Tan WC, *et al.* Highly stretchable and sensitive photodetectors based on hybrid graphene and graphene quantum dots. ACS Appl Mater Interfaces, 2016, 8: 466–471
18 Leintz R, Bond JW. Can the RUVIS reflected UV imaging system visualize fingerprint corrosion on brass cartridge casings postfiring? J Forensic Sci, 2013, 58: 772–775
19 Cheong P, Chang KF, Lai YH, *et al.* A ZigBee-based wireless sensor network node for ultraviolet detection of flame. IEEE Trans Ind Electron, 2011, 58: 5271–5277
20 Tian W, Lu H, Li L. Nanoscale ultraviolet photodetectors based on onedimensional metal oxide nanostructures. Nano Res, 2015, 8: 382–405
21 Li L, Gu L, Lou Z, *et al.* ZnO quantum dot decorated Zn_2SnO_4 nanowire heterojunction photodetectors with drastic performance enhancement and flexible ultraviolet image sensors. ACS Nano, 2017, 11: 4067–4076
22 Zhai T, Fang X, Liao M, *et al.* A comprehensive review of one-dimensional metal-oxide nanostructure photodetectors. Sensors, 2009, 9: 6504–6529
23 Lou Z, Li L, Shen G. High-performance rigid and flexible ultraviolet photodetectors with single-crystalline $ZnGa_2O_4$ nanowires. Nano Res, 2015, 8: 2162–2169
24 Huang S, Guo CF, Zhang X, *et al.* Buckled tin oxide nanobelt webs as highly stretchable and transparent photosensors. Small, 2015, 11: 5712–5718
25 Kim D, Shin G, Yoon J, *et al.* High performance stretchable UV sensor arrays of SnO_2 nanowires. Nanotechnology, 2013, 24: 315502
26 Gutruf P, Zeller E, Walia S, *et al.* Stretchable and tunable microtectonic ZnO-based sensors and photonics. Small, 2015, 11: 4532–4539
27 Hu L, Yan J, Liao M, *et al.* Ultrahigh external quantum efficiency from thin SnO_2 nanowire ultraviolet photodetectors. Small, 2011, 7: 1012–1017
28 Soci C, Zhang A, Xiang B, *et al.* ZnO nanowire UV photodetectors with high internal gain. Nano Lett, 2007, 7: 1003–1009
29 Zhang D, Li C, Han S, *et al.* Ultraviolet photodetection properties of indium oxide nanowires. Appl Phys A-Mater Sci Processing, 2003, 77: 163–166
30 Tsai TY, Chang SJ, Weng WY, *et al.* A visible-blind TiO_2 nanowire photodetector. J Electrochem Soc, 2012, 159: J132–J135
31 Prades JD, Hernandez-Ramirez F, Jimenez-Diaz R, *et al.* The effects of electron–hole separation on the photoconductivity of individual metal oxide nanowires. Nanotechnology, 2008, 19: 465501
32 Liu X, Gu L, Zhang Q, *et al.* All-printable band-edge modulated ZnO nanowire photodetectors with ultra-high detectivity. Nat Commun, 2014, 5: 4007
33 Zhao B, Wang F, Chen H, *et al.* Solar-blind avalanche photodetector based on single ZnO–Ga_2O_3 core–shell microwire. Nano Lett, 2015, 15: 3988–3993
34 Lin CH, Chen RS, Chen TT, *et al.* High photocurrent gain in SnO_2 nanowires. Appl Phys Lett, 2008, 93: 112115
35 Wu JM, Kuo CH. Ultraviolet photodetectors made from SnO_2 nanowires. Thin Solid Films, 2009, 517: 3870–3873
36 Li L, Lou Z, Shen G. Hierarchical CdS nanowires based rigid and flexible photodetectors with ultrahigh sensitivity. ACS Appl Mater Interfaces, 2015, 7: 23507–23514
37 Deng K, Li L. CdS nanoscale photodetectors. Adv Mater, 2014, 26: 2619–2635
38 Li H, Wang X, Xu J, *et al.* One-dimensional CdS nanostructures: A promising candidate for optoelectronics. Adv Mater, 2013, 25: 3017–3037
39 Li L, Wu P, Fang X, *et al.* Single-crystalline CdS nanobelts for

excellent field-emitters and ultrahigh quantum-efficiency photodetectors. Adv Mater, 2010, 22: 3161–3165
40 Chen S, Lou Z, Chen D, *et al.* Polymer-enhanced highly stretchable conductive fiber strain sensor used for electronic data gloves. Adv Mater Technol, 2016, 1: 1600136
41 Zhang X, Xie Y, Zhao Q, *et al.* 1-D coordination polymer template approach to CdS and HgS aligned-nanowire bundles. New J Chem, 2003, 27: 827–830
42 Qiu J, Li X, He W, *et al.* The growth mechanism and optical properties of ultralong ZnO nanorod arrays with a high aspect ratio by a preheating hydrothermal method. Nanotechnology, 2009, 20: 155603
43 Xu F, Zhu Y. Highly conductive and stretchable silver nanowire conductors. Adv Mater, 2012, 24: 5117–5122
44 Cheng B, Xu J, Ouyang Z, *et al.* Individual Ohmic contacted ZnO/Zn_2SnO_4 radial heterostructured nanowires as photodetectors with a broad-spectral-response: Injection of electrons into/from interface states. J Mater Chem C, 2014, 2: 1808
45 Xu Y, Schoonen MAA. The absolute energy positions of conduction and valence bands of selected semiconducting minerals. Am Miner, 2000, 85: 543–556
46 Kamiya Y, Naito Y, Hirose T, *et al.* Sorption and partial molar volume of gases in poly(dimethyl siloxane). J Polym Sci B Polym Phys, 1990, 28: 1297–1308
47 Liu Z, Huang H, Liang B, *et al.* Zn_2GeO_4 and $In_2Ge_2O_7$ nanowire mats based ultraviolet photodetectors on rigid and flexible substrates. Opt Express, 2012, 20: 2982
48 Hu L, Kim HS, Lee JY, *et al.* Scalable coating and properties of transparent, flexible, silver nanowire electrodes. ACS Nano, 2010, 4: 2955–2963
49 Poquillon D, Viguier B, Andrieu E. Experimental data about mechanical behaviour during compression tests for various matted fibres. J Mater Sci, 2005, 40: 5963–5970
50 Slobodian P, Riha P, Lengalova A, *et al.* Compressive stress-electrical conductivity characteristics of multiwall carbon nanotube networks. J Mater Sci, 2011, 46: 3186–3190

Acknowledgements This work was supported by the National Natural Science Foundation of China (61625404, 61888102 and 61574132), and the Key Research Program of Frontier Sciences, CAS (QYZDY-SSW-JWC004).

Author contributions Li L, Lou Z and Shen G proposed the idea; Li L and Lou Z designed and engineered the samples; Li L, Lou Z, Chen H, and Shi R performed the experiments; Li L, Lou Z and Shen G wrote the paper. All authors contributed to the general discussion.

Conflict of interest The authors declare no conflict of interest.

Supplementary information Experimental details are available in the online version of this paper.

Ludong Li received his bachelor degree in materials physics from Qingdao University in 2013. Now he is a PhD candidate in Prof. Shen's group. His current research interest focuses on the flexible and stretchable photodetectors, image sensors and energy devices.

Guozhen Shen received his BSc degree (1999) in chemistry from Anhui Normal University and PhD degree (2003) in chemistry from the University of Science and technology of China. He joined the Institute of Semiconductors, Chinese Academy of Sciences as a Professor in 2013. His current research focuses on the flexible electronics and printable electronics, including transistors, photodetectors, sensors and flexible energy storage and conversion devices.

可拉伸SnO_2-CdS交叠纳米线薄膜紫外光电探测器

李禄东[1,2†], 娄正[1†], 陈浩然[1,2], 史瑞龙[1,2], 沈国震[1,2*]

摘要 快速响应、可拉伸紫外光电探测器在可穿戴电子和嵌入式生物医学器件中有广泛应用. 然而, 对于大多数基于传统二元氧化物纳米线的光电探测器来说, 大量表面缺陷产生的俘获中心使得探测器表现出非常慢的响应速度. 本工作利用SnO_2-CdS交叠纳米线薄膜作为敏感材料, 通过多重模板抽滤法制备出了响应速率显著提高的可拉伸紫外光电探测器. 研究表明, 与纯SnO_2纳米线光电探测器相比, 基于交叠纳米线的光电探测器具有更低的暗电流和更大的响应速率(>100倍). 此外, 本文还讨论了相关的载流子产生和传输的机制. 另外, 由于在预拉伸循环过程中纳米线/PDMS层的表面形成了波浪形的褶皱, SnO_2-CdS交叠纳米线薄膜光电探测器在50%的拉伸应变下展现出了优异的电学稳定性和拉伸循环特性, 在150次拉伸循环后仍未表现出明显的性能衰减. 作为一种简单有效的制备快速响应可拉伸紫外光电探测器的策略, 交叠纳米线结构也可以被应用到其他纳米线组合中, 比如ZnO-CdS交叠纳米线. 金属氧化物-CdS纳米线交叠结构制备能够快速响应的紫外光电探测器是一种普适的方法, 其在未来的可拉伸和可穿戴光电器件中具有巨大的应用潜力.

